Bull. Mater. Sci., Vol. 36, No. 6, November 2013, pp. 997–1004. © Indian Academy of Sciences.

Optical, magnetic and structural characterization of $Zn_{1-x}Co_xO$ nanoparticles synthesized by solvothermal method

TOKEER AHMAD*, SARVARI KHATOON and KELSEY COOLAHAN†
Department of Chemistry, Jamia Millia Islamia, New Delhi 110 025, India
†Department of Physics and Astronomy, Rowan University, 201 Mullica Hill Road, Glassboro, NJ 08028, USA

MS received 4 May 2012; revised 3 October 2012

Abstract. **Nanoparticles of Co-doped ZnO with 3·8, 7·2 and 11·5 wt% were synthesized by solvothermal method through oxalate precursor route. X-ray diffraction studies showed the formation of hexagonal ZnO structure for $x = 0{\cdot}038$, however, secondary phase of Co_3O_4 arises on increasing the Co content up to 11·5%. Transmission electron microscopic studies showed that particles are in the nano-metric regime and the grain size decreases on increasing the Co concentration. Optical reflectance measurements showed an energy bandgap, which decreases on increasing Co concentration. Specific surface area of these nanoparticles was found to be very high and comes out to be 97·6, 112·1 and 603·8 m^2g^{-1}, respectively. All the solid solutions showed paramagnetism with weak antiferromagnetic interactions. It is seen that the antiferromagnetic interaction increases on increasing Co concentration.**

Keywords. **Co-doped ZnO nanoparticles; transmission electron microscopy; surface area; magnetic properties.**

1. Introduction

In recent years, dilute magnetic semiconductors have attracted considerable attention, both theoretically and experimentally, due to their potential technological applications in the field of optoelectronics, magnetoelectronics and microwave devices. After theoretical prediction of room temperature ferromagnetism in transition metal-doped ZnO and GaN (Dietl *et al* 2000), ZnO based dilute magnetic semiconductors have been extensively studied for potential applications in the field of spintronics and magneto–optic components (Sato and Yoshida 2002; Sharma *et al* 2003; Sluiter *et al* 2005). Several groups have studied the growth of Co-doped ZnO films, which is a good candidate with high Curie temperature (Sato and Yoshida 2000, 2001). Huge magneto-optical effect is observed in Co-doped ZnO films (Ando *et al* 2001). Ferromagnetic behaviour is observed in Co-doped ZnO films with T_c above 280 K synthesized by pulsed laser deposition (Ueda *et al* 2001). However, Jin *et al* (2001) found no indication of ferromagnetism synthesized by laser molecular beam epitaxy (Jin *et al* 2001). Room temperature ferromagnetism with high magnetization and large negative magnetoresistance was found in Co-doped ZnO inhomogeneous magnetic semiconductors (Yan *et al* 2004). 25% Co-doped ZnO thin films deposited on sapphire substrates by pulsed laser deposition were found to be ferromagnetic at room temperature (Rode *et al* 2003). Most of the previous investigations showed that Co-doped ZnO nanoparticles were synthesized by physical techniques. This paper describes our efforts to synthesize Co-doped ZnO nanoparticles using modified solvothermal method through oxalate precursor route because, one can obtain more homogeneous product by this route at a relatively low temperature. The nanoparticles have been characterized by thermogravimetry, X-ray diffraction, transmission electron microscopy and surface area studies. The detailed optical and magnetic properties have been studied and discussed.

2. Experimental

$Zn_{1-x}Co_xO$ ($x = 0{\cdot}038$, $0{\cdot}072$ and $0{\cdot}115$) nanoparticles were synthesized by solvothermal method through oxalate precursor route. All the metal solutions were prepared in double-distilled water of 0·1 M concentration. Stoichiometric amount of zinc sulphate heptahydrate (Qualigens, 99%) and cobalt acetate tetrahydrate (Merck, 99%) were well mixed in 500 mL round-bottom flask and stirred for about 30 min. The mixture was precipitated with 75 mL aqueous solution of diammonium oxalate (Merck, 99%). A light pink suspension was immediately formed. 75 mL of ethanol (Changshu Yangyuan Chemical, China, 99·9%) was also added to the reaction mixture to form the low-boiling azeotrope with water. The reaction mixture was refluxed at about 80 °C for 12 h in a closed environment so that the volume of the reaction mixture remains constant. The precipitate was recovered by centrifugation, washed several times with water and finally with acetone. The precipitates were dried in an oven at 55 °C and finally ground to powder. $Zn_{1-x}Co_xO$ nanoparticles were obtained by thermal decomposition of the precursor at 450 °C for 6 h in air. Figure 1

*Author for correspondence (tahmad3@jmi.ac.in)

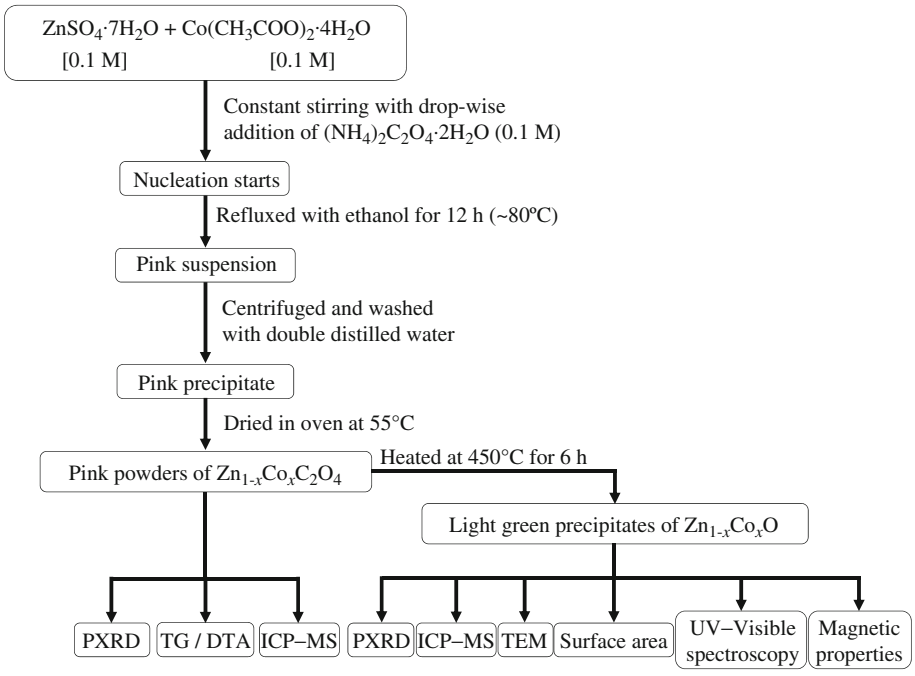

Figure 1. Flowchart for solvothermal synthesis of $Zn_{1-x}Co_xO$ ($x = 0{\cdot}038$, $0{\cdot}072$ and $0{\cdot}115$) nanoparticles.

shows flow chart for the solvothermal synthesis of Co-doped ZnO nanoparticles.

The crystalline phases of the samples were characterized by powder X-ray diffraction using Bruker D8 advance X-ray diffractometer with Ni-filtered CuKα radiation. Normal scans were recorded with a step size of $0{\cdot}050°$ and step time of 1 s. Thermal decomposition of the oxalate precursors were studied by thermogravimetry and differential thermal analysis with an EXSTAR 6000 instrument in nitrogen atmosphere at a heating rate of 10 °C min^{-1} with alumina as a reference sample.

Composition of solid solutions was estimated by inductively coupled plasma–mass spectrometry analysis using Agilent 7500a inductively coupled plasma with MS detector. The crystal size and morphology have been studied by transmission electron microscopy using FEI Technai G^2 20 transmission electron microscope with an accelerating voltage of 200 kV. The specimens were prepared by dispersing the samples in ethanol and placing a drop of the dispersed sample in a copper grid.

Room temperature optical properties were recorded on ocean optics lambda-25 UV–Visible spectrophotometer in the reflectance mode. The powder samples were compacted to pellets. The energy bandgap of these nanoparticles can be further calculated by the reflection spectra using Kubelka–Munk function, $F(R)$ (Kortum 1969):

$$F(R) = (1 - R)^2/2R,$$

where R is the diffuse reflectance.

Specific surface area of the samples was determined by Quantachrome instruments (Model NOVA 2000e surface area and pore size analyser). Samples were degassed at 250 °C for 3 h in vacuum because of the removal of any adsorbed gases. After degassing, specific surface areas were obtained from the nitrogen adsorption experiments measured at 77·35 K. Magnetic properties of as-grown $Zn_{1-x}Co_xO$ ($x = 0{\cdot}038$, $0{\cdot}072$ and $0{\cdot}115$) were investigated using quantum design physical properties measurement system.

3. Results and discussion

Figure 2 shows TG and DTA curves recorded at 10 °C min^{-1} up to 500 °C for the thermal decomposition of 3·6, 7·6 and 11·9% Co-doped zinc oxalate precursors, respectively, in nitrogen atmosphere. From TG curves, it is observed that the precursor remains stable up to a temperature of about 110 °C. TG curves display two well-defined weight loss steps. The shapes of thermal decomposition curve in the temperature range 110–190 °C shows a single step dehydration reaction. The measured weight loss for this decomposition stage is about 18% of the total weight resulting in the elimination of two water molecules (reaction 1). Corresponding to this dehydration step, single broad endotherm in the temperature range of 110–205 °C is seen in DTA curve. The anhydrous oxalate was nearly thermally stable up to 345 °C after which, it starts to decompose in the second TG step. Heating from 345 to 410 °C, results in complete collapse of the material to its corresponding oxides with the simultaneous evolution of CO and CO_2 (reactions 2 and 3, respectively). The measured weight loss in this stage is about 36%, which is almost equal to that of the theoretical value. The decarbonylation

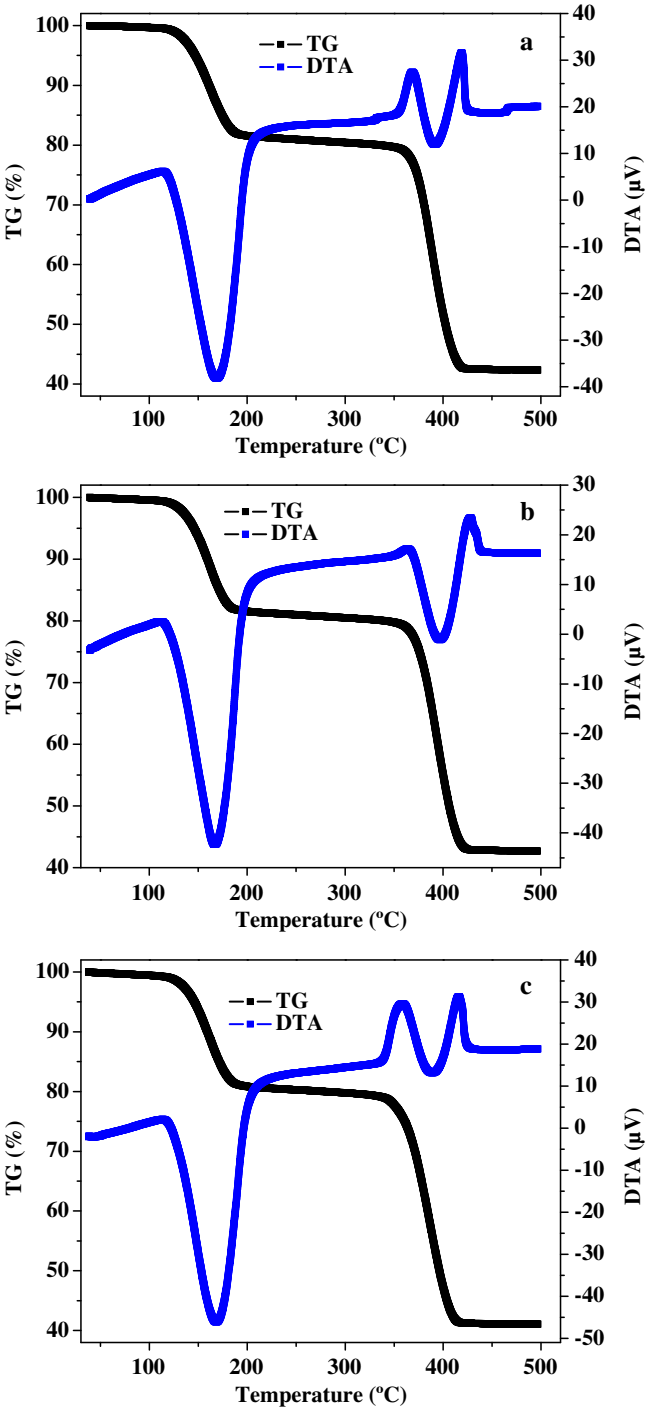

Figure 2. TG/DTA curves of $Zn_{1-x}Co_xC_2O_4$ nanoparticles for $x =$ (**a**) 0·036, (**b**) 0·076 and (**c**) 0·119.

and decarboxylation reactions are characterized by the two exothermic DTA peaks at around 365 and 405 °C, respectively, attributed to the decomposition of anhydrous oxalate with the formation of carbonate followed by the formation of its corresponding oxides. The residual weight corresponds to Co-doped ZnO, which is confirmed by powder X-ray diffraction studies. On the basis of TG and DTA results, brown precipitate of $Zn_{1-x}Co_xO$ ($x = 0{\cdot}038$, 0·072 and 0·115) nanoparticles were obtained by the decomposition of precursors at 450 °C for 6 h.

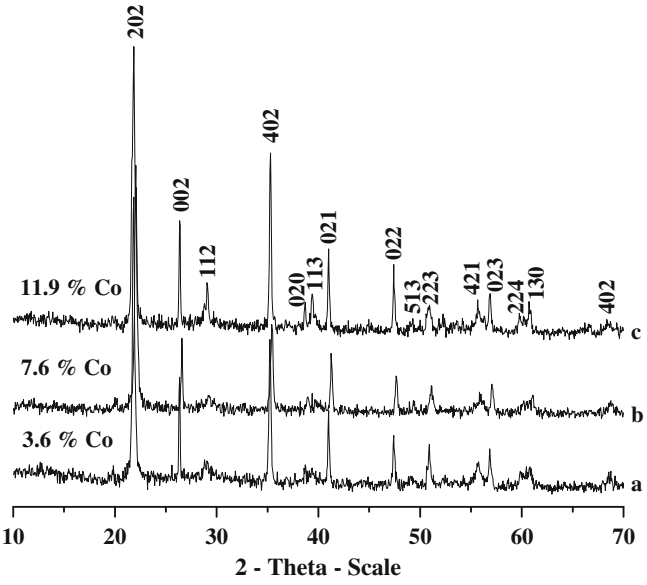

Figure 3. Powder X-ray diffraction patterns of $Zn_{1-x}Co_xC_2O_4$ nanoparticles for $x =$ (**a**) 0·036, (**b**) 0·076 and (**c**) 0·119.

$$Zn_{1-x}Co_xC_2O_4{\cdot}2H_2O \xrightarrow{110-190\ ^\circ C} Zn_{1-x}Co_xC_2O_4 + 2H_2O, \quad (1)$$

$$Zn_{1-x}Co_xC_2O_4 \xrightarrow{345-375\ ^\circ C} Zn_{1-x}Co_xCO_3 + CO\uparrow, \quad (2)$$

$$Zn_{1-x}Co_xCO_3 \xrightarrow{375-410\ ^\circ C} Zn_{1-x}Co_xO + CO_2\uparrow. \quad (3)$$

Figure 3 shows powder X-ray diffraction pattern of Co-doped zinc oxalate in the angular range of $10^\circ < 2\theta < 70^\circ$. All the reflections could be assigned to the monoclinic zinc oxalate dihydrate (JCPDS no. 25-1029). However, peaks are slightly shifted to higher angle of diffraction which may be attributed to the Co-doping in ZnC_2O_4 host lattice. Intensity and crystallinity of peaks increase on increasing the cobalt concentration.

Powder X-ray diffraction pattern of Co-doped ZnO nanoparticles are shown in figure 4. The pattern shows that for $x = 0{\cdot}038$, all the diffraction peaks are indexed on the basis of hexagonal structure of ZnO (JCPDS no. 80-0075) with slight shifting of the reflection towards higher angle. Contraction of the lattice may be due to the incorporation of Co^{2+} in ZnO lattice sites as the ionic radii of Co^{2+} (0·58 Å) is smaller than Zn^{2+} (0·60 Å), beyond which the additional peaks of Co_3O_4 appeared, which shows that the phase segregation occurred in this system. The intensity of the impurity peaks goes on increasing as Co content in the sample increased. XRD results showed that the solubility limit of Co

ions in ZnO is less than 7·2% because, phase separations to ZnO and Co_3O_4 were clearly seen.

Composition of $Zn_{1-x}Co_xC_2O_4{\cdot}2H_2O$ and its corresponding oxides was estimated using ICP studies. Results showed that percentage of Co in solid solution is less than that used during the synthesis. However, conversion of oxalate to oxide did not alter the composition. The composition of the samples was taken as estimated from ICP. ICP data and estimated molecular formula using ICP studies are shown in table 1.

Morphology and particle size of the Co-doped ZnO nanoparticles have been estimated by transmission electron microscopic (TEM) analysis. Figure 5 shows TEM micrographs of Co-doped ZnO nanoparticles synthesized at 450 °C, indicating the hexagonal nanoparticles with an average grain size of 17, 15 and 11 nm, respectively. For 3·8% Co-doped ZnO, the particles are distributed in the range of 9–30 nm with an average grain size of 17 nm (figure 5(a)). For 7·2% Co, particles lie in the size range of 7–18 nm with a maximum frequency at 15 nm (figure 5(b)). Few bigger particles (28 nm) are also seen in the micrograph, which may be due to the aggregation or overlapping of smaller particles. On further increasing the Co concentration to 11·5%, the maximum frequency of particles is found to be 11 nm (figure 5(c)).

Optical characterization of Co-doped ZnO nanoparticles in UV–Visible range was carried out by measuring the reflectance at room temperature. Figure 6 shows reflectance spectra indicating three well-defined absorption edges at around 570, 620 and 660 nm. These edges are assigned to the *d–d* crystal field transitions of the tetrahedrally coordinated Co^{2+} ions. The appearance of these transitions clearly suggests that the doped Co^{2+} is in high-spin state (Kim and Park 2002; Ramachandran *et al* 2004; Hays *et al* 2007). Since the spectral data show the characteristic transitions of the tetrahedrally coordinated Co^{2+} ions, it can be concluded that Co substituted Zn^{2+} ions. The direct bandgap energies of these nanoparticles were estimated from Kubelka–Munk relation by plotting $[F(R) \times E]^2$ vs energy in electron volts (eV). Linear part of the curve was extrapolated to $[F(R) \times E]^2 = 0$, to calculate the bandgap as shown in figure 7.

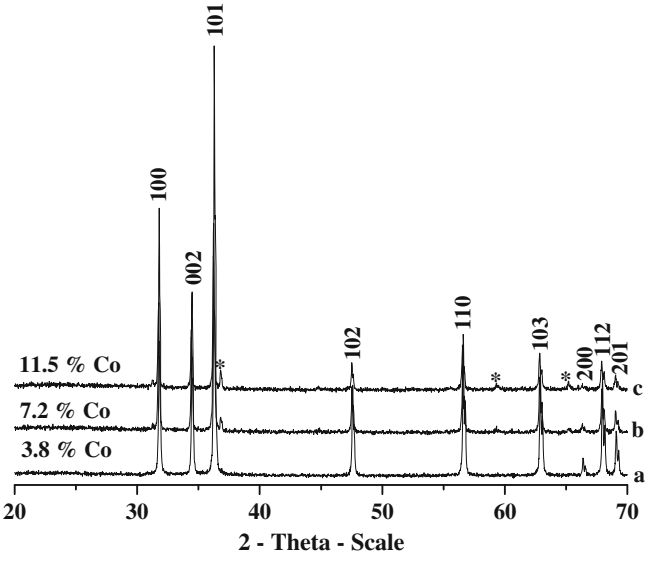

Figure 4. Powder X-ray diffraction patterns of $Zn_{1-x}Co_xO$ nanoparticles for $x =$ (**a**) 0·038, (**b**) 0·072 and (**c**) 0·115.

The estimated bandgap comes out to be 3·27, 3·25 and 3·21 eV, respectively, which decreases on increasing the Co ion concentration. The red shift of the bandgap with insertion of Co ion in ZnO matrix has already been reported (Kim and Park 2002; Hays *et al* 2007). This may be due to *sp–d* exchange interactions between the band electrons and the localized *d* electrons of Co^{2+} ions.

Specific surface area of these nanoparticles was calculated by BET plots in the P/P_0 range of 0·05–0·30 using multipoint BET equation and found to be 97·6, 112·1 and 603·8 m^2g^{-1}, respectively, which increases on increasing Co concentration. The increase in surface area may be due to the decrease in particle size. The surface area of Co-doped ZnO is very high in comparison to the earlier report (He *et al* 2012). To the best of our knowledge, this is the first report on high surface area of Co-doped ZnO nanoparticles. N_2 adsorption–desorption isotherms of these nanoparticles show type-IV curve with H3 hysteresis (figure 8), attributed to the presence of mesopores (Sing *et al* 1985). However, the hysteresis area is narrow, indicating the mesopores of smaller size. Pore radius of these nanoparticles have been estimated using BJH method (figure 9) and comes out to be 18·29, 18·27 and 16·37 Å, respectively. The increase in surface area and decrease in pore radius may be due to the formation of smaller average grain size due to the increase in disorder with the incorporation of Co ions into ZnO matrix (Barick *et al* 2008). Table 2 displays BET surface area, BJH pore radius and particle size of Co-doped ZnO nanoparticles.

For proper investigation of the magnetic properties of Co-doped ZnO nanoparticles, temperature dependence of the molar magnetic susceptibility and inverse molar magnetic susceptibility has been estimated at a constant magnetic field of 1 kOe as shown in figure 10. The molar magnetic

Table 1. Estimated composition of $Zn_{1-x}Co_xC_2O_4$ and $Zn_{1-x}Co_xO$ using ICP–MS studies.

Loaded Co content	ICP–MS for $Zn_{1-x}Co_xC_2O_4$		Estimated composition	ICP–MS for $Zn_{1-x}Co_xO$		Estimated composition
	Zn (%)	Co (%)		Zn (%)	Co (%)	
5	96·41	3·59	$Zn_{0.964}Co_{0.036}C_2O_4{\cdot}2H_2O$	96·21	3·79	$Zn_{0.962}Co_{0.038}O$
10	92·43	7·57	$Zn_{0.924}Co_{0.076}C_2O_4{\cdot}2H_2O$	92·80	7·20	$Zn_{0.928}Co_{0.072}O$
15	88·08	11·92	$Zn_{0.881}Co_{0.119}C_2O_4{\cdot}2H_2O$	88·48	11·52	$Zn_{0.885}Co_{0.115}O$

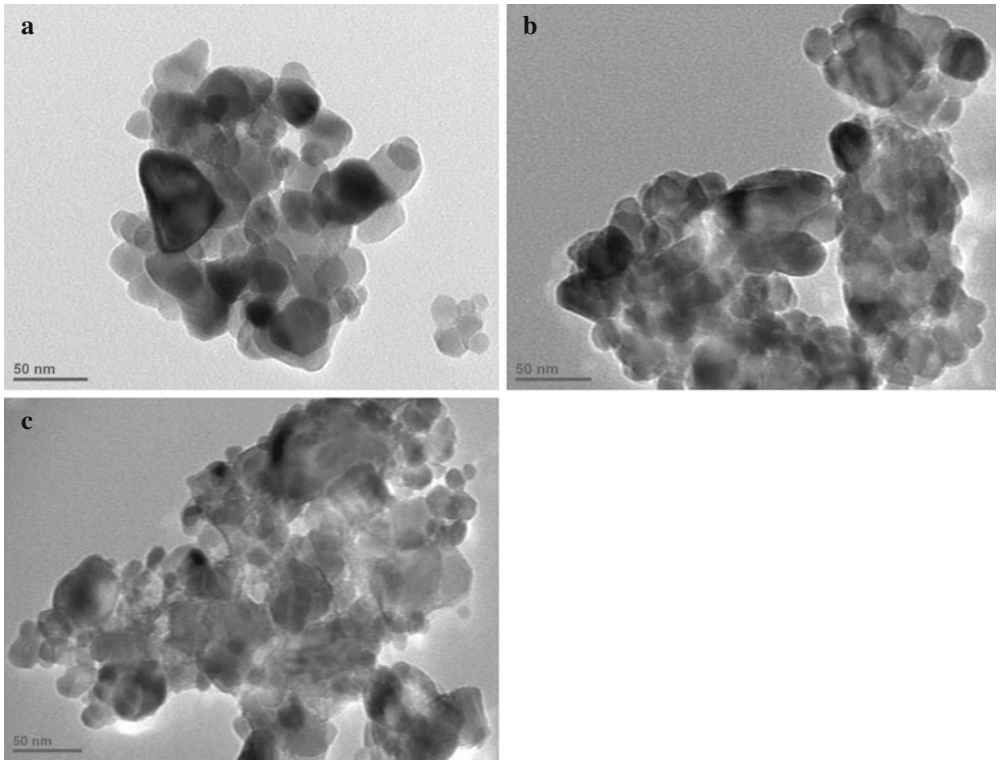

Figure 5. TEM micrographs of $Zn_{1-x}Co_xO$ nanoparticles for $x =$ (**a**) 0·038, (**b**) 0·072 and (**c**) 0·115.

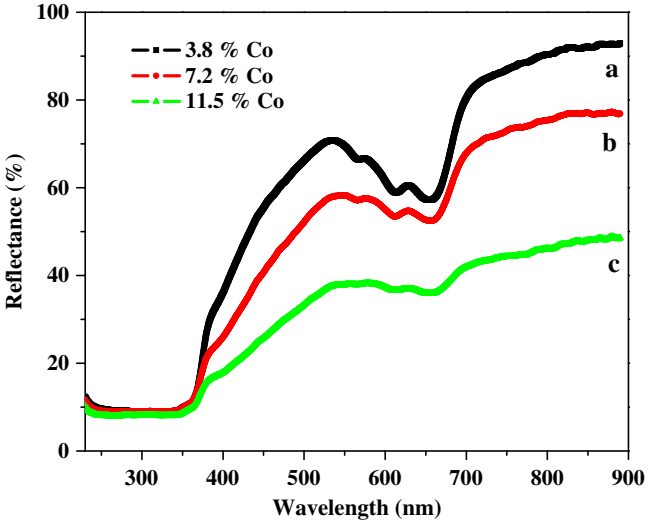

Figure 6. UV–Visible reflectance spectra of $Zn_{1-x}Co_xO$ ($x =$ 0·038, 0·072 and 0·115) nanoparticles.

susceptibility decreases continuously with increasing temperature, indicating the paramagnetic behaviour of the samples. The inverse susceptibility vs temperature plot is fitted with a Curie–Weiss linear relation for the high temperature region:

$$\chi = C/(T + \theta),$$

where χ is the magnetic susceptibility, C the paramagnetic Curie constant and θ the Curie–Weiss temperature. Extrapolation of the inverse susceptibility data in the high temperature region gave negative Curie–Weiss temperatures of −38, −20 and −98 K, respectively. The negative value of θ indicates antiferromagnetic interactions between Co ions. Such antiferromagnetic interactions were also reported earlier by several researchers in Co- and Mn-doped ZnO systems (Mandal *et al* 2006, 2007). The non-systematic Curie–Weiss temperatures could be associated with the anomalies among the transition metals, cobalt exhibits complex magnetic properties because of extensive spin–orbit coupling and possibility of the co-existence of high-spin and low-spin configurations. The former leads to a substantial deviation from the g values and the latter leads to temperature-dependent de-population of high-spin exited states.

The effective magnetic moment of the solid solutions have been calculated using the equation,

$$\mu_{\text{eff}} = \sqrt{8C},$$

where C is the Curie constant.

The calculated effective magnetic moment of 3·8% Co-doped ZnO solid solutions was found to be 3·77 μ_B/Co^{2+} and is consistent with the expected effective magnetic moment of Co^{2+} (3·87 μ_B/Co^{2+}). These results show that introduction of Co^{2+} in ZnO host lattice is not sufficient to achieve ferromagnetism. On increasing the Co concentration to 7·2 and 11·5%, effective magnetic moment

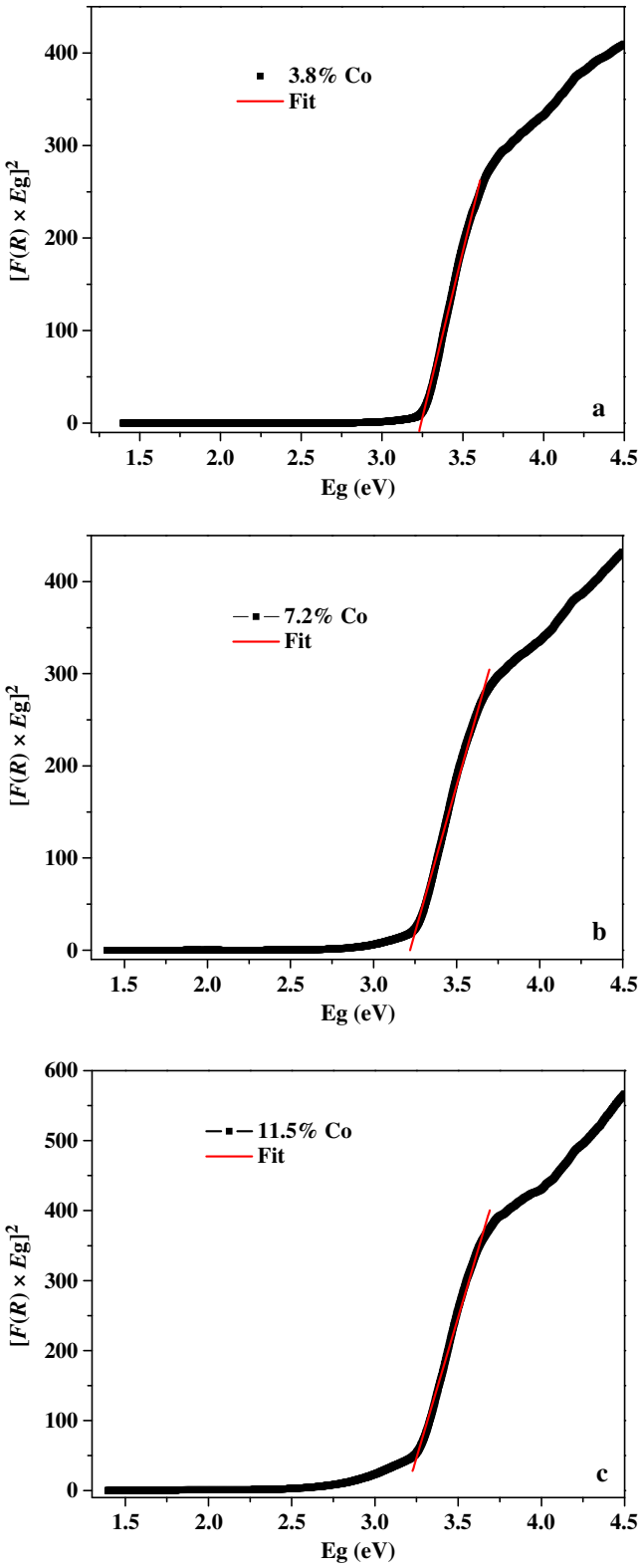

Figure 7. $[F(R) \times E]^2$ vs energy plot for direct bandgap determination of $Zn_{1-x}Co_xO$ nanoparticles for $x =$ (**a**) 0·038, (**b**) 0·072 and (**c**) 0·115.

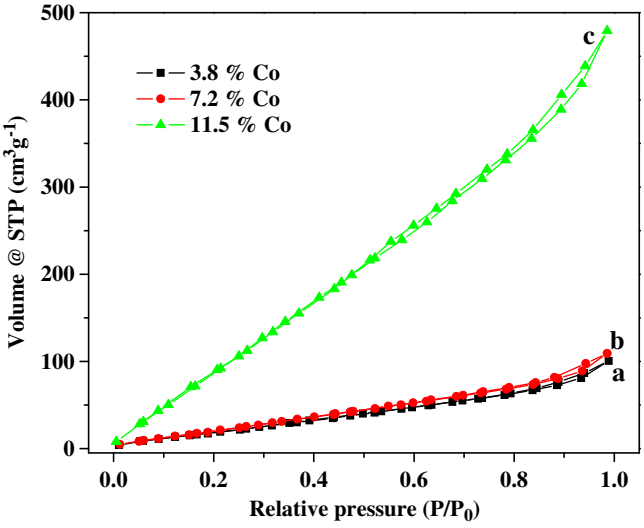

Figure 8. Nitrogen adsorption–desorption isotherms of $Zn_{1-x}Co_xO$ ($x = 0{\cdot}038$, 0·072 and 0·115) nanoparticles.

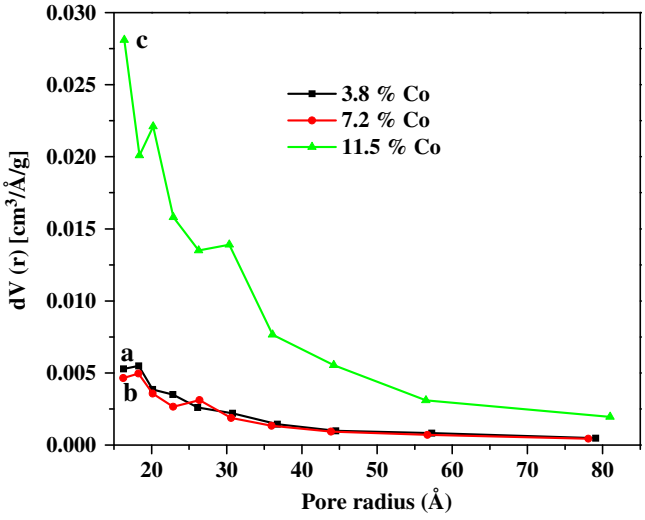

Figure 9. BJH plots of $Zn_{1-x}Co_xO$ ($x = 0{\cdot}038$, 0·072 and 0·115) nanoparticles.

Table 2. BET surface area, BJH pore radius and TEM particle size of $Zn_{1-x}Co_xO$ ($x = 0{\cdot}038$, 0·072 and 0·115) nanoparticles.

Composition	TEM particle size (nm)	BET surface area (m^2g^{-1})	BJH pore radius (Å)
$Zn_{0.962}Co_{0.038}O$	17	97·6	18·29
$Zn_{0.928}Co_{0.072}O$	15	112·1	18·27
$Zn_{0.885}Co_{0.115}O$	11	603·8	16·37

reduced to 2·72 and 2·66 μ_B/Co^{2+}, respectively. This may be due to some mixed valence state of cobalt, which is already studied in XRD results. The decrease in magnetic moment on increasing the Co concentration may be due to some antiferromagnetic super-exchange interactions which takes place within the neighbouring Co^{2+} ions through O^{2-} ions. Similar decrease in magnetic moment with increasing

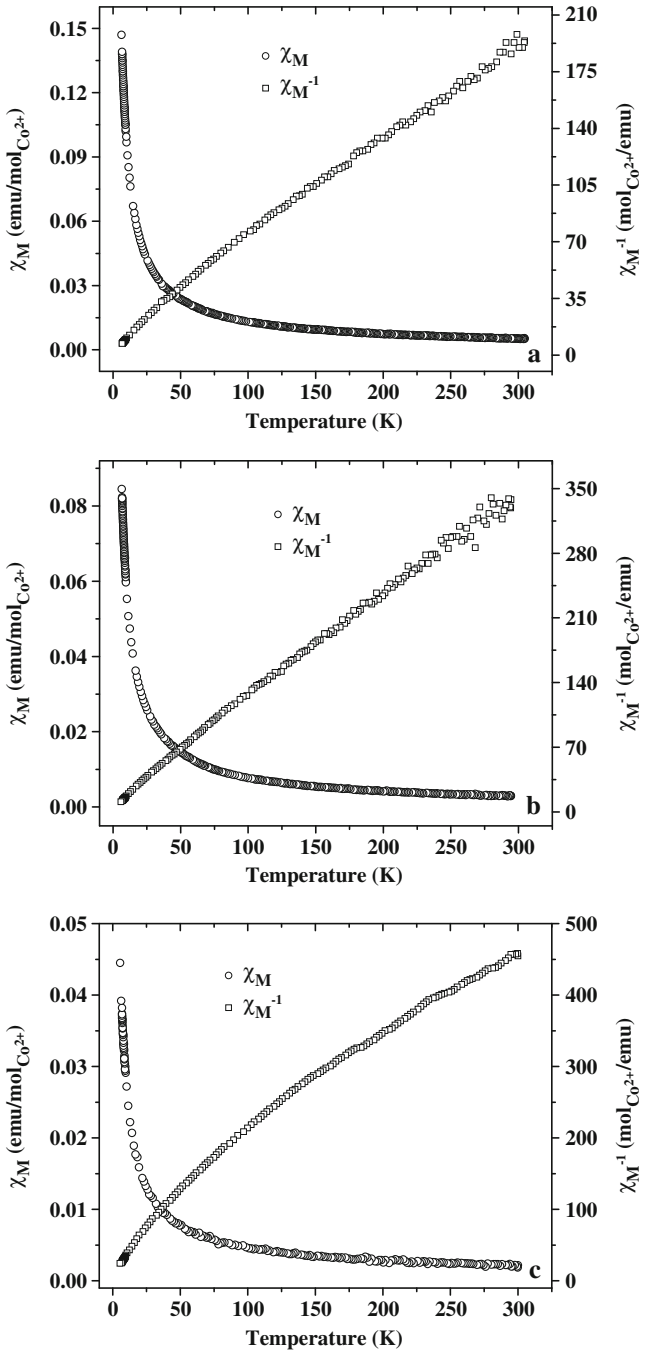

Figure 10. Temperature dependence of molar magnetic susceptibility and inverse susceptibility plots of $Zn_{1-x}Co_xO$ ($x = 0{\cdot}038$, $0{\cdot}072$ and $0{\cdot}115$) nanoparticles measured at a magnetic field of 1 kOe.

transition metal concentration is reported earlier in 3*d* elements doped oxide semiconductors (Ogale *et al* 2003; Wang *et al* 2006). Figure 11 shows magnetization curves measured at 5 K, which confirmed the paramagnetic behaviour of these solutions. Magnetic studies confirmed that all the Co-doped ZnO nanoparticles show paramagnetism with weak antiferromagnetic interactions.

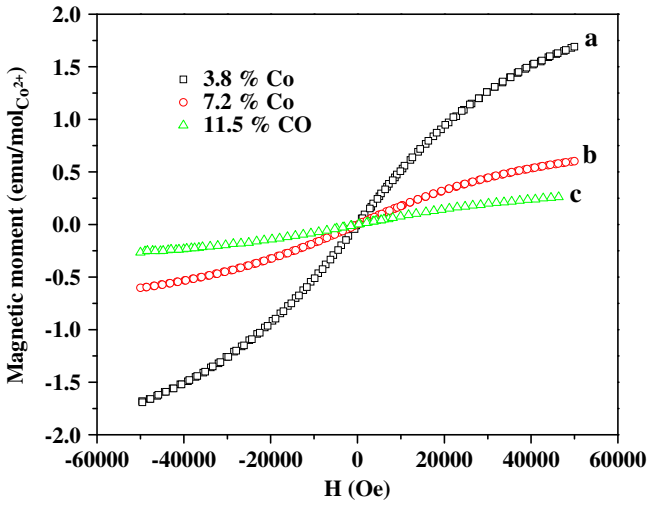

Figure 11. Magnetic field vs magnetic moment plots of $Zn_{1-x}Co_xO$ ($x = 0{\cdot}038$, $0{\cdot}072$ and $0{\cdot}115$) nanoparticles measured at a temperature of 5 K.

4. Conclusions

We have synthesized $Zn_{1-x}Co_xO$ nanoparticles with $0{\cdot}038 \leq x \leq 0{\cdot}115$ using solvothermal method. No secondary phase was observed in XRD pattern for 3·8% Co, however, secondary phase of Co_3O_4 arises on increasing Co concentration. For low doping level ($x = 0{\cdot}038$), tetrahedral Co^{2+} ions seem to be incorporated into Zn^{2+} matrix, as evidenced from X-ray diffraction, ICP, reflectance spectroscopy and magnetic measurements. Particle size decreases from 17 to 11 nm and surface area increases from 97·6 to 603·8 m^2g^{-1} on increasing the Co concentration in Zn matrix. Magnetic measurements revealed the paramagnetic behaviour of all these solid solutions along with weak antiferromagnetic interactions.

Acknowledgements

One of the authors (TA) thanks CSIR, Govt of India, for financial support (research project no. 01(2448)/10EMR-II). (SK) thanks UGC and CSIR for research fellowships. The authors thank Prof K V Ramanujachary, Rowan University, USA, for inductively coupled plasma–mass spectrophotometry and magnetic measurements. The authors also thank AIIMS, New Delhi, for transmission electron microscopy facility.

References

Ando K, Saito H, Jin Z, Fukumura T, Kawasaki M, Matsumoto Y and Koinuma H 2001 *Appl. Phys. Lett*. **78** 2700

Barick K C, Aslam M, Dravid V P and Bahadur D 2008 *J. Phys. Chem. C* **112** 15163

Dietl T, Ohno H, Matsukura F, Cibert J and Ferrand D 2000 *Science* **287** 1019

Hays J *et al* 2007 *J. Phys. Condens. Matter*. **19** 266203
He R, Hocking R K and Tsuzuki T 2012 *Mater. Chem. Phys*. **132** 1035
Jin Z *et al* 2001 *Appl. Phys. Lett*. **78** 3824
Kim K J and Park Y R 2002 *Appl. Phys. Lett*. **81** 1420
Kortum G 1969 *Reflectance spectroscopy: principles, methods, applications* (New York: Springer)
Mandal S K, Das A K, Nath T K, Karmakar D and Satpati B 2006 *J. Appl. Phys*. **100** 104315
Mandal S K, Nath T K, Das A K and Karmakar D 2007 *J. Appl. Phys*. **101** 063913
Ogale S B, Choudhary R J, Buban J P and Shinde S R 2003 *Phys. Rev. Lett*. **91** 077205
Ramachandran S, Tiwari A and Nayaran J 2004 *Appl. Phys. Lett*. **84** 5255
Rode K, Anane A, Mattana R, Contour J P, Durand O and Le Bourgeois R 2003 *J. Appl. Phys*. **93** 7676
Sato K and Yoshida H K 2000 *Jpn J. Appl. Phys*. **39** L555
Sato K and Yoshida H K 2001 *Jpn J. Appl. Phys*. **40** L334
Sato K and Yoshida H K 2002 *Semicond. Sci. Technol*. **17** 367
Sharma P *et al* 2003 *Nat. Mater*. **2** 673
Sing K S W, Everett D H, Haul R A W, Moscou L, Pierotti R A, Rouquerol J and Siemieniewska T 1985 *Pure Appl. Chem.* **57** 603
Sluiter M H F, Kawazoe Y, Sharma P, Inoue A, Raju A R, Rout C and Waghmare U V 2005 *Phys. Rev. Lett*. **94** 187204
Ueda K, Tabata H and Kawai T 2001 *Appl. Phys. Lett*. **79** 988
Wang Y X, Liu H, Li Z Q, Zhang X X, Zheng R K and Ringer S P 2006 *Appl. Phys. Lett*. **89** 042511
Yan S S *et al* 2004 *Appl. Phys. Lett*. **84** 2376